Journal Pre-proof

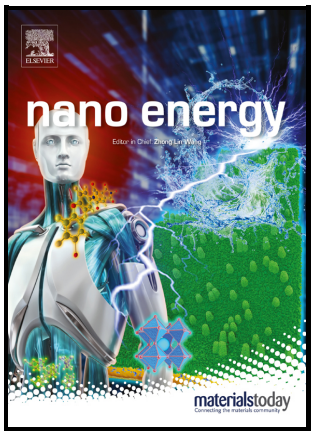

2D $Ti_3C_2T_x$ MXene-Based Light-Driven Actuator with Integrated Structure for Self-Powered Multi-Modal Intelligent Perception Assisted by Neural Network

Jiahao Zhou, Huamin Chen, Zhihao Wu, Peidi Zhou, Minghua You, Chan Zheng, Qiaohang Guo, Zhou Li, Mingcen Weng

PII: S2211-2855(24)01304-1

DOI: https://doi.org/10.1016/j.nanoen.2024.110552

Reference: NANOEN110552

To appear in: *Nano Energy*

Received date: 11 October 2024
Revised date: 21 November 2024
Accepted date: 5 December 2024

Please cite this article as: Jiahao Zhou, Huamin Chen, Zhihao Wu, Peidi Zhou, Minghua You, Chan Zheng, Qiaohang Guo, Zhou Li and Mingcen Weng, 2D $Ti_3C_2T_x$ MXene-Based Light-Driven Actuator with Integrated Structure for Self-Powered Multi-Modal Intelligent Perception Assisted by Neural Network, *Nano Energy,* (2024) doi:https://doi.org/10.1016/j.nanoen.2024.110552

2D $Ti_3C_2T_x$ MXene-Based Light-Driven Actuator with Integrated Structure for Self-Powered Multi-Modal Intelligent Perception Assisted by Neural Network

Jiahao Zhou[1], Huamin Chen[2, 3, *], Zhihao Wu[4], Peidi Zhou[5], Minghua You[1], Chan Zheng[1], Qiaohang Guo[6], Zhou Li[2, *], Mingcen Weng[1, *]

1 Institute of Biology and Chemistry, Fujian University of Technology, Fuzhou, 350118, China.

2 Beijing Institute of Nanoenergy and Nanosystems Chinese Academy of Sciences Beijing 100083 China

3 Fujian Key Laboratory of Functional Marine Sensing Materials Minjiang University Fuzhou 350108 China

4 College of Computer and Data Science, Fuzhou University, Fuzhou 350116, China

5 Institute of Smart Marine and Engineering, Fujian University of Technology, Fuzhou, Fujian, 350118, China

6 School of Materials Science and Engineering, Fujian University of Technology, Fuzhou, 350118, China

* Corresponding authors:

Huamin Chen, chenhuamin@mju.edu.cn

Zhou Li, zli@binn.cas.cn

Mingcen Weng, wengmc@fjut.edu.cn

Abstract

Conventional $Ti_3C_2T_x$ MXene-based actuators, due to their lack of human-like self-perception capability, have hindered soft robots from progressing toward intelligent robot-environment interactions. Strategies to reconcile environmental stimulus-response actuation and self-powered multi-modal intelligent perception remain challenging. Here, we have designed a flexible actuator with a P-N couple structure. Wherein, the $Ti_3C_2T_x$

MXene-chitin nanofibers (MCHF) composite film prepared by vacuum-assisted self-assembly was utilized as the N-type photothermal layer, and the PEDOT:PSS/PET film was utilized as the P-type thermal-expansion layer. Based on the thermoelectric and electronegative properties of the MCHF composite film, we propose two strategies to combine the light-driven actuation mechanism with the photo-thermoelectric effect (PTE) and triboelectric effect to endow the light-driven actuator perception capabilities. Based on the PTE effect, the MCHF-based bilayer film can be directly utilized as a PTE generator (Seebeck coefficient of 23.3 μV K^{-1}) to simultaneously achieve light-driven actuation and self-powered relative-temperature perception. When utilized as a triboelectric electrode (maximum output voltage of 144.7 V), the MCHF layer can trigger the triboelectric effect with the actuation force of the light-driven actuator, thus realizing self-powered material perception. Finally, we demonstrated an intelligent gripper capable of synergizing light-driven actuation and self-powered multi-modal perception by compactly integrating these two strategies, which can recognize susceptible signals accurately (accuracy of 98%) with the assistance of a neural network. This work is promising to facilitate the intelligent interaction of $Ti_3C_2T_x$ MXene-based soft robots with variable environments.

Keywords:

Self-powered sensor; triboelectric nanogenerator; soft actuator; photo-thermoelectric effect; $Ti_3C_2T_x$ MXene

1. Introduction

Benefiting from the capability to proactively convert complex external stimuli (e.g.,

light, electricity, humidity, magnetism, and pressure) into mechanical deformations, flexible actuators have fueled the continued development of soft robots in areas such as artificial muscles, smart homes, conveyance, human-machine interaction, and drug delivery [1-5]. As an inexhaustible clean resource, light can be utilized as a stimulus energy for flexibly driving flexible actuators from a remote location, which is why light-driven actuators have received extensive research [6-8]. Conventional actuators can trigger the dual effects of asymmetric thermal expansion and thermal dehydration by transferring heat from the photothermal-conversion layer to the thermal-expansion layer, which is a well-established light-driven actuation mechanism [9-11]. However, the inability of conventional light-driven actuators to perceive autonomously forces most soft robots to rely on embedding external power and sensing modules to acquire stimulus response information, at the expense of lightweight and remote actuation sensitivity [12-15]. Therefore, there is an urgent need to find suitable materials to develop photothermal-conversion layers that combine excellent photothermal-conversion efficiency, hydrophilicity, thermal conductivity, and electrical properties to endow light-driven actuators with actuation and perception capabilities.

As a 2D transition metal carbide/nitride with high thermal conductivity, $Ti_3C_2T_x$ MXene can effectively absorb and utilize light energy over a wide spectral range, resulting in a unique localized surface plasmon resonance (LSPR) effect and near-complete internal photothermal-conversion efficiency [16, 17]. And the abundant hydrophilic functional groups on the nanosheet surface allow $Ti_3C_2T_x$ MXene to enhance the light-driven actuation by desorbing water molecules [18, 19]. Most importantly, the

metal conductivity of $Ti_3C_2T_x$ MXene is probably the highest among all 2D materials (e.g., graphene, graphene derivatives, and MoS_2, etc.), which opens up unlimited possibilities for a wide range of self-powered perception applications for light-driven actuators. Unfortunately, although many $Ti_3C_2T_x$ MXene light-driven actuators with excellent light-driven performance based on asymmetric structural designs have been reported, these studies have not fully utilized the high conductivity properties of $Ti_3C_2T_x$ MXene to improve the actuator's environmental perception capability. [20-22]. Therefore, there is an urgent need to develop lightweight actuators with integrated tele-autonomous actuation and multi-modal environmental perception, which is the key to realizing intelligent robot-environment interaction for soft robots. To address the challenge of developing $Ti_3C_2T_x$ MXene-based actuators with integrated perception functions, targeted development of actuator structures as well as coordinating the synergistic operation of light-driven actuation and self-powered perception mechanisms are required.

Similar to the light-driven actuation mechanism, the photo-thermoelectric effect (PTE) effect is a noncontact energy conversion mechanism that converts photothermal energy into electric energy [23, 24]. A few light-driven actuators with self-powered relative-temperature perception have recently been developed based on the PTE effect [10, 25-27]. For example, Zhou et al. developed a P-type PTE actuator based on graphene-graphene oxide/biaxially oriented polypropylene bilayer actuation material, which was applied to self-powered conveyance and bionic hand [25]. Based on this study, Gu et al. developed a light-driven actuator with both PTE relative-temperature perception and

visual temperature sensing by coating paper with a P-type graphite layer and thermochromic dye [26]. This strategy of generating relative-temperature perception signals by constructing temperature differences on the actuators provides new ideas for the development of self-powered light-driven actuators with autonomous perception. Nonetheless, the unipolar thermoelectric structures slightly restrict the electrode position design and actuation flexibility of the light-driven actuator. Compared to P-N couple structures, unipolar thermoelectric structures are more difficult to optimize the PTE performance of actuators. Not only that, considering that soft robots need to contact different object surfaces frequently, it is imperative to develop novel contact perception functions in addition to the existing noncontact relative-temperature perception function. Different from the PTE effect, the triboelectric effect is a contact self-powered perception mechanism that is widely found between materials with different surface potentials [28-30]. During contact-separation processes, these materials can spontaneously generate voltage signals by coupling contact electrification and electrostatic induction. We note that the light-driven actuator's mechanical deformation induced by the light stimulus can be utilized as a contact-separation trigger for the synchronized triboelectric effect. The high surface electronegativity of $Ti_3C_2T_x$ MXene also makes the $Ti_3C_2T_x$ MXene-based photothermal-conversion layer ideally suitable as an actuation electrode for triboelectric sensing [31, 32]. The innovative strategy of combining the light-driven mechanism with the PTE effect and triboelectric effect is expected to break through the impossibility of $Ti_3C_2T_x$ MXene-based light-driven actuators to realize contact and noncontact multi-modal environment perception.

Herein, we developed a light-driven actuator with a bilayer P-N couple structure and proposed an "actuation-temperature perception-material perception" integrated strategy (Fig. 1). Specifically, we fabricated a self-standing N-type $Ti_3C_2T_x$ MXene-chitin nanofibers (MCHF) composite film via vacuum filtration-assisted self-assembly as a passive layer for photothermal conversion and triboelectric generation. By in-situ attachment of a P-type thermoelectric film with a large coefficient of thermal expansion (CTE) to the MCHF composite film, a MCHF-based bilayer film was constructed. First, thanks to the excellent PTE performance of the MCHF-based bilayer film (Seebeck coefficient of 23.3 $\mu V\ K^{-1}$), we developed a PTE actuator with mutually unaffected light-driven deformation performance (bending curvature of 0.59 cm^{-1}) and self-powered relative-temperature perception by constructing temperature differences on the MCHF layer. The series-connected smart curtains designed based on the PTE actuators can spontaneously open and output synchronized thermoelectric signals in response to NIR light. Second, the contact-separation triboelectric nanogenerator (TENG) constructed with the MCHF-based bilayer film as the triboelectric negative electrode was demonstrated to possess excellent output performance (output voltage of 144.7 V). Based on these performances, we developed a triboelectric actuator with self-powered material perception by utilizing the bending actuation force as a contact-separation trigger. The triboelectric actuator can undergo different charge transfers when contacting different objects and thus spontaneously outputs the corresponding voltage signals. Finally, by compactly integrating the PTE actuator and the triboelectric actuator, we de-

veloped an intelligent gripper that can realize the synergistic effect of light-driven actuation and multi-modal (relative temperature/material) perception. Assisted by a multilayer perceptron (MLP) neural network, the environmentally susceptible signals can be more accurately recognized (average accuracy of 98%). This work provides a simple and practical strategy for intelligent interaction between $Ti_3C_2T_x$ MXene-based soft robots and complex environments.

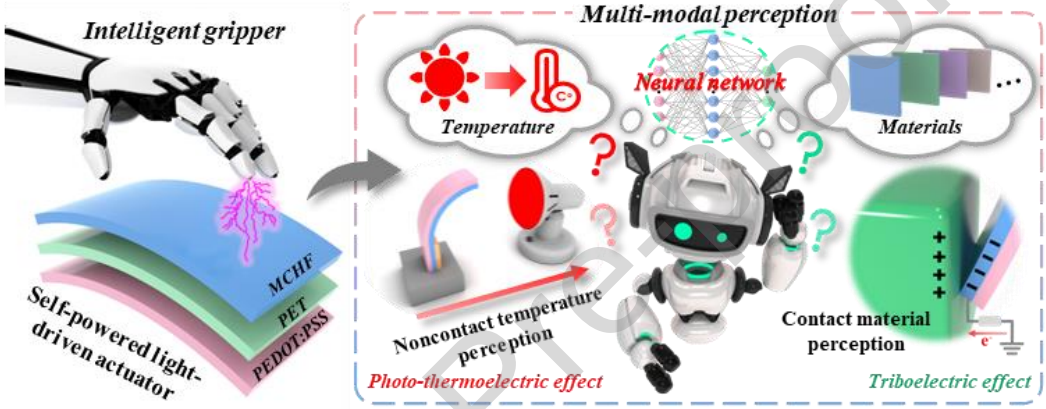

Fig. 1 Conceptual illustration of the neural network-assisted "actuation-temperature perception-material perception" integrated strategy proposed based on the light-driven actuators with bilayer P-N couple structure.

2. Result and Discussion

2.1 Fabrication and Characterization of the MCHF Composite Film

MXenes, an emerging class of two-dimensional transition metal carbides and/or nitrides, have been extensively utilized in flexible light-driven actuators recently due to their excellent conductivity and photothermal conversion performance [33-36]. However, the intrinsic toughness deficiency and susceptibility to oxidization of $Ti_3C_2T_x$ MXene pose significant challenges to $Ti_3C_2T_x$ MXene-based actuators [37, 38]. Therefore, we attempted to modulate the robust performance of $Ti_3C_2T_x$ MXene nanosheets

by introducing chitin nanofibers (CHF) derived from crustaceans. The fabrication process of the MCHF composite film is illustrated schematically in Fig. 2a. The $Ti_3C_2T_x$ MXene nanosheets obtained by mild etching and ultrasonic exfoliation were self-assembled with CHF under the assistance of vacuum filtration, thus constructing the MCHF composite film with a multilayer structure. After drying, the self-standing MCHF composite film can be easily removed from filter paper. The MCHF composite films with different mass ratios are shown in Fig. S1 (Supporting Information). After measurement, these MCHF composite films exhibited ultra-thin thicknesses of about 30 μm. TEM and SEM were first used to characterize the MCHF composite film in order to observe its microstructure. As shown in Fig. 2b, the prepared $Ti_3C_2T_x$ MXene nanosheets exhibit a typical two-dimensional layered structure with a transverse size of about 2 nm. The abundance of surface functional groups (e.g., -O, -OH, and -F) endows $Ti_3C_2T_x$ MXene nanosheets with excellent hydrophilicity, allowing them to be well dispersed in water without the formation of aggregates, as shown in Fig. S2 (Supporting Information) [39]. While CHF exhibit a cobweb-like porous network structure with a diameter of about 50-100 nm and a length of more than 100 μm, as shown in Fig. S3 (Supporting Information). CHF also have hydrophilic functional groups represented by -OH, which provide a large number of active sites for its hydrogen bonding interaction with $Ti_3C_2T_x$ MXene nanosheets (Fig. S4, Supporting Information) [40, 41]. Under the extensive hydrogen bonding, the $Ti_3C_2T_x$ MXene nanosheets and CHF tightly intertwined, thus forming a stable solution state (Fig. 2c). Thanks to the abundance of functional groups and high aspect content, CHF can easily penetrate into the interlayers of

$Ti_3C_2T_x$ MXene nanosheets and form a multilayer network structure, as shown in Fig. 2d-e and Fig. S5 (Supporting Information).

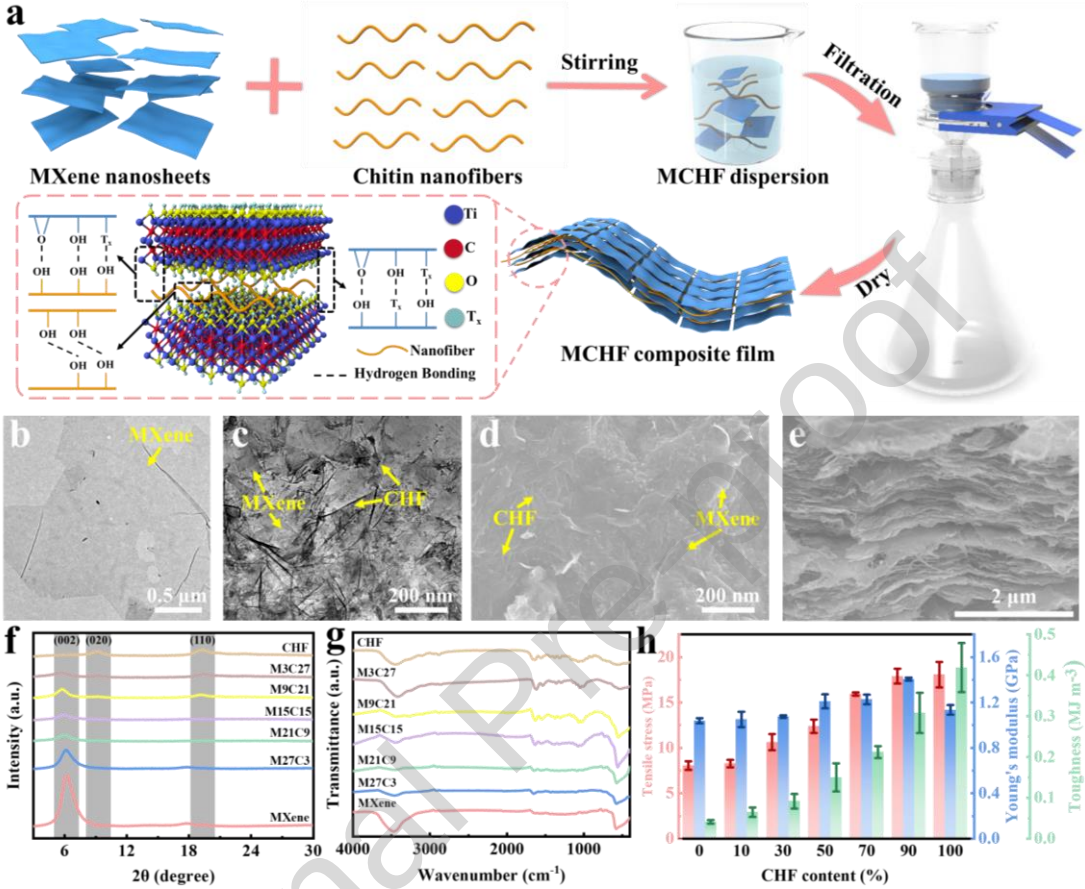

Fig. 2 Demonstration of the fabrication and characterization of the MCHF composite film. (a) Schematic illustration of the fabrication process of the MCHF composite film. TEM image of the $Ti_3C_2T_x$ MXene nanosheets (b) and MCHF composite film (c). (d) Surface SEM image of the MCHF composite film. (e) Cross-sectional SEM image of the MCHF composite film. (f) The XRD spectra of $Ti_3C_2T_x$ MXene nanosheets, CHF, and the MCHF composite films with different mass ratios. (g) The FT-IR spectra of $Ti_3C_2T_x$ MXene nanosheets, CHF, and the MCHF composite films with different mass ratios. (h) Mechanical properties of the MCHF composite film with different mass ratios.

Then, the crystal structures of $Ti_3C_2T_x$ MXene, CHF, and the MCHF composite films with different mass ratios were investigated through XRD, as shown in Fig. 2f. The diffraction peaks of CHF appeared around 9.3° and 19.3°, corresponding to the (020) and (110) crystal planes of α-chitin, respectively [42]. And a typical diffraction peak of $Ti_3C_2T_x$ MXene appears around $2\theta = 6.2°$, which corresponds to the (002) characteristic crystal plane [43]. With the increase in CHF content, the (002) diffraction peak shifts towards a smaller diffraction angle. For example, the (002) diffraction peak of $Ti_3C_2T_x$ MXene shifted from 6.20° to 5.62° in M3C27 composite film. Based on the Bragg's law formula (Note S1, Supporting Information), the layer spacings of M30, M27C3, M21C9, M15C5, M9C21, and M3C27 composite films can be calculated as 1.42 nm, 1.44 nm, 1.46 nm, 1.51 nm, 1.53 nm, and 1.57 nm, respectively (Fig. S6, Supporting Informaiton). Apparently, the introduction of CHF increases the layer spacing between $Ti_3C_2T_x$ MXene nanosheets, thus weakening their over-stacking. In addition, the increase in CHF content will also gradually enhance the intensity of the (020) and (110) diffraction peaks of the MCHF composite film [41]. Subsequently, we further investigated the chemical compositions of these materials using FT-IR. As can be seen from the FT-IR spectra shown in Fig. 2g, the $Ti_3C_2T_x$ MXene nanosheets exhibit characteristic peaks at around 3,450 cm^{-1}, 1,635 cm^{-1}, and 550 cm^{-1}, corresponding to -OH, C-F, and Ti-O bonds, respectively [44]. As for CHF, in addition to the characteristic peak corresponding to the -OH group at 3450 cm^{-1}, it also exhibits characteristic peaks corresponding to the amide I, amide II, and amide III bands of chitin at around 1,637

cm^{-1}, 1,555 cm^{-1}, and 1,313 cm^{-1}, respectively [45]. Notably, the diffraction peaks representing the O-H tensile vibration of the MCHF composite films progressively shift to lower wavenumbers as the CHF content increases. This is largely due to the enhanced hydrogen bonding interaction's influence on the O-H tensile vibration [46]. Finally, the mechanical properties of MCHF composite film with different mass ratios were measured and analyzed, as shown in Fig. 2h and Fig. S7 (Supporting Information). Before the introduction of CHF, the tensile stress, Young's modulus and toughness of the pure $Ti_3C_2T_x$ MXene film were only 8.05 MPa, 1.04 GPa, and 0.041 MJ m^{-3}, respectively. This demonstrates its obvious brittle characteristics. CHF, on the other hand, showed satisfactory mechanical properties with tensile strength, Young's modulus, and toughness of 18.06 MPa, 1.14 GPa, and 0.42 MJ m^{-3}, respectively. Therefore, CHF proved to be an ideal mechanically enhanced biomass filler. After measurement, the mechanical properties of the MCHF composite films were significantly enhanced. For example, the tensile stress, Young's modulus and toughness of the M21C9 composite film can respectively reach 10.63 MPa, 1.08 GPa and 0.092 MJ m^{-3}, which are 32.05 %, 3.85 % and 124.39 % higher than those of the pure $Ti_3C_2T_x$ MXene film. In addition, the fracture strain, specific hardness, and specific tensile strength of the MCHF composite film were also much higher than those of the pure $Ti_3C_2T_x$ MXene film. The enhanced comprehensive mechanical properties of the MCHF composite films are mainly attributed to the fact that CHF fills the interlayer of $Ti_3C_2T_x$ MXene nanosheets through extensive hydrogen bonding, thus improving the mechanical defects such as uneven stress distribution and insufficient toughness of pure $Ti_3C_2T_x$ MXene films [47]. As a result the

MCHF composite films exhibit excellent flexibility and mechanical stability in the folded state and in the 300-time bending test, as shown in Fig. S8 (Supporting Information) and Fig. S9 (Supporting Information). Benefiting from the high conductivity of $Ti_3C_2T_x$ MXene nanosheets, the MCHF composite films with low CHF content also maintain excellent conductivity. For example, the conductivity of M27C3 and M21C9 composite films can reach 269.5 S cm^{-1} and 150.9 S cm^{-1}, respectively (Fig. S10, Supporting Information).

2.2 Thermoelectric Performance of the MCHF/PET/PEDOT:PSS Bilayer Film

As an N-type two-dimensional material, $Ti_3C_2T_x$ MXene is beginning to be utilized to regulate the comprehensive performance of thermoelectric materials due to its unique layered structure, high conductivity, and low lattice thermal conductivity [48, 49]. However, the over-stacking effect within $Ti_3C_2T_x$ MXene may limit carrier transport and reduce active sites [50-52]. And the intrinsically low Seebeck coefficient of $Ti_3C_2T_x$ MXene has not been effectively addressed [53]. Thus, we have inserted CHF networks into the compact lamellar structure of $Ti_3C_2T_x$ MXene nanosheets by hydrogen-bonded self-assembly in an attempt to improve $Ti_3C_2T_x$ MXene's Seebeck coefficient. As shown in Fig. S11 (Supporting Information), a bilateral two-electrode thermoelectric measurement structure was introduced. The thermoelectric properties of the MCHF composite films with different mass ratios were evaluated by setting nine different temperature segments (Fig. S12, Supporting Information). The summary of the measurement results is exhibited in Fig. S13 (Supporting Information). It can be seen

that the Seebeck coefficients of the CHF-modified MCHF composite films are all superior to that of the pure $Ti_3C_2T_x$ MXene film. Among them, the M21C9 composite film has the highest Seebeck coefficient of -13.5 μV K^{-1}, which is enhanced by 27% compared to the pure $Ti_3C_2T_x$ MXene film (-10.6 μV K^{-1}). Notably, with the increase in CHF content, the Seebeck coefficients of MCHF composite films show an increasing and then decreasing trend. This is because the doping modification of a small amount of CHF can effectively mitigate the over-stacking of $Ti_3C_2T_x$ MXene nanosheets, thus providing more channels for carrier transport. But when the CHF content exceeds a certain equilibrium point, its insulating properties will inhibit the conductivity of the MCHF composite film. As a result, it is difficult for the MCHF composite films to simultaneously achieve high mechanical properties and high thermoelectric efficiency. To better realize the subsequent relative-temperature perception, we chose the M21C9 composite film with the highest Seebeck coefficient as the photothermal layer of the light-driven actuator. As a result, the M21C9 composite film was selected for subsequent performance measurements and applications. However, the thermoelectric properties of the individual MCHF composite film are still unsatisfactory, and it is not capable of independently accomplishing light-driven actuation. To address these problems, we directly in-situ attached a commercial P-type poly(3,4-ethylenedioxythiophene):polystyrene sulfonate/polyethylene terephthalate (PEDOT:PSS/PET) film to the MCHF composite film surface via acrylic ester. The PEDOT:PSS/PET film possesses a 15.1 μV K^{-1} Seebeck coefficient (Fig. S14, Supporting Information) and a large CTE [46]. Silver adhesive was then brushed on top, thus constructing a conductive channel

between these two films. In this way, a self-standing MCHF/PET/PEDOT:PSS bilayer film with a bilayer P-N couple structure was easily constructed, as shown in Fig. S15 (Supporting Information). This structural design not only avoids complicated preparation for PN junction but also retains flexibility not available with conventional thermoelectric devices. Additionally, it allows the assembly of the electrodes in a more flexible position compared to using separate P/N thermoelectric films.

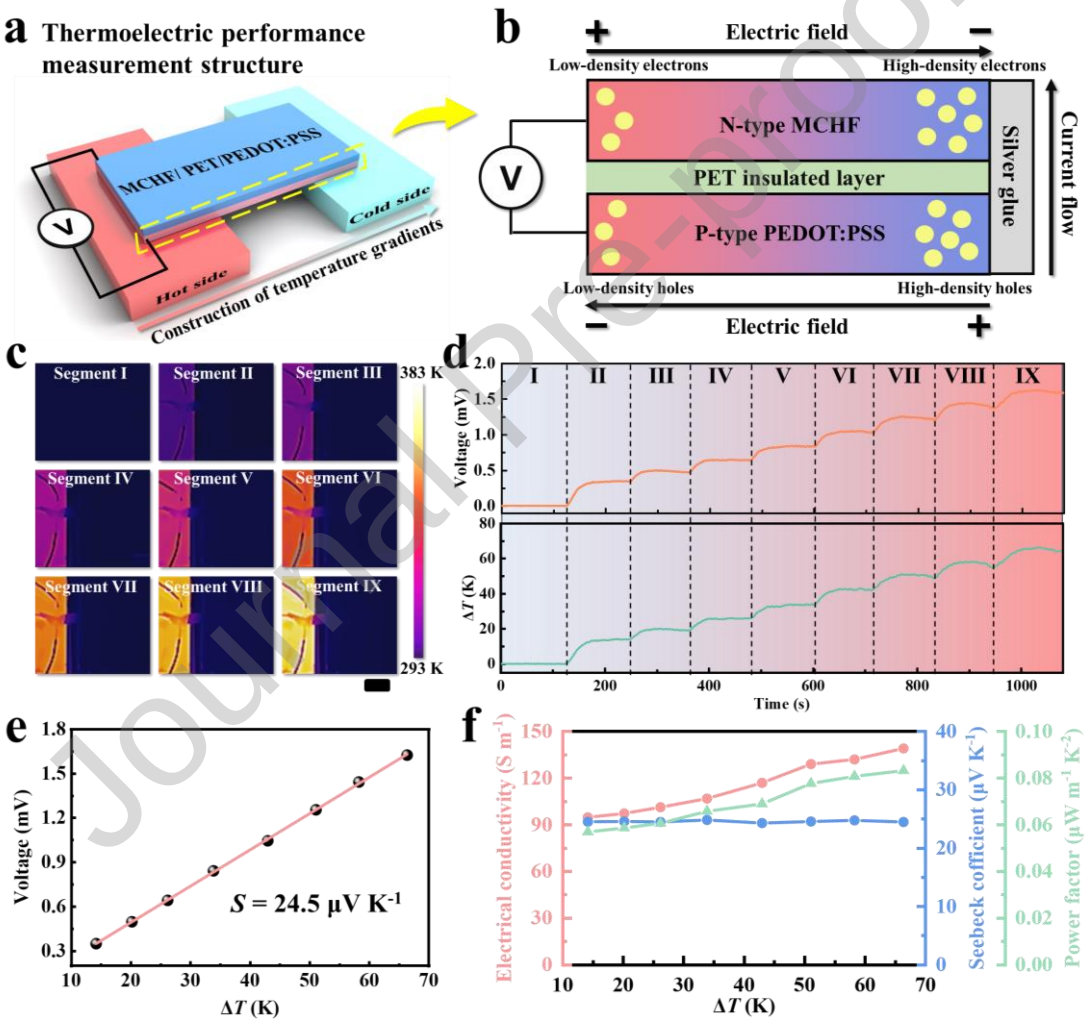

Fig. 3 Demonstration of the thermoelectric performance of the MCHF/PET/PEDOT:PSS bilayer film. (a) Schematic illustration of the thermoelectric performance measurement structure. (b) Schematic illustration of the thermoelectric signal genera-

tion mechanism of the MCHF/PET/PEDOT:PSS bilayer film. (c) Infrared thermal images of the nine temperature segments in the thermoelectric performance measurement. (d) Output voltage and temperature difference of the MCHF/PET/PEDOT:PSS bilayer film at different temperature differences. (e) Seebeck coefficient of the MCHF/PET/PEDOT:PSS bilayer film. (f) The comprehensive thermoelectric performance of the MCHF/PET/PEDOT:PSS bilayer film.

To harvest thermoelectric signals from the MCHF/PET/PEDOT:PSS bilayer film, an ipsilateral two-electrode measurement structure was designed as shown in Fig. 3a and Fig. S16 (Supporting Information). When a temperature difference is applied along the length of the MCHF/PET/PEDOT:PSS bilayer film, the electrons inside the N-type MCHF layer and the holes inside the P-type PEDOT:PSS layer will move diffusively from the hot side to the cold side, resulting in an electric potential (Fig. 3b). Fig. 3c displays the infrared thermal images of the nine temperature segments in the thermoelectric performance measurement of the MCHF/PET/PEDOT:PSS bilayer film. As can be seen in Fig. 3d, the output voltage and the temperature difference between the hot and cold sides of the MCHF/PET/PEDOT:PSS bilayer film exhibit a consistent step-like trend. This trend demonstrates that the MCHF/PET/PEDOT:PSS bilayer film can effectively convert the temperature difference into electrical energy based on the Seebeck effect. Furthermore, the output voltage of the MCHF/PET/PEDOT:PSS bilayer film exhibits an excellent linear relationship with the temperature difference, and its fitted Seebeck coefficient can reach 24.5 $\mu V\ K^{-1}$ calculated by linear fitting (Fig. 3e).

These stable internal electron and hole transport properties of the MCHF/PET/PEDOT:PSS bilayer film contribute to the reliability of subsequent perception. According to the thermoelectric figure of merit formula (Note S2, Supporting Inforamation), conductivity is another important parameter that affects the overall thermoelectric properties besides the Seebeck coefficient. Therefore, the conductivity of the MCHF/PET/PEDOT:PSS bilayer film was measured at different temperature differences, as shown in Fig. 3f. As the hot-side temperature increased, the conductivity of the MCHF/PET/PEDOT:PSS bilayer film rose from 94.7 S m^{-1} (ΔT = 14.2 K) to 139.0 S m^{-1} (ΔT = 66.4 K), which demonstrates the semiconducting fundamental property. And the corresponding power factor also increased from 0.056 μW m^{-1} K^{-2} to 0.083 μW m^{-1} K^{-2}. Compared with the pure $Ti_3C_2T_x$ MXene film, the MCHF/PET/PEDOT:PSS bilayer film obtained by modification treatment and structural design exhibits excellent comprehensive thermoelectric performance.

2.3 Light-Driven actuation and dynamic PTE Performance of the MCHF/PET/PEDOT:PSS-Based PTE Actuator with Relative-Temperature Perception

Photothermal conversion is a more remote and flexible strategy for generating temperature differences, compared to direct thermal contact. The dense structure of pure $Ti_3C_2T_x$ MXene film hinders the light from entering the interior, thus limiting the utilization of light [6]. Thanks to the weakening of the Ti3C2Tx MXene over-stacking by CHF, the MCHF composite film can exhibit excellent LSPR effect and incident light absorption [17]. The photothermal conversion efficiency η_p can be approximated as: $\eta_p = \frac{Ah(T_S - T_0)}{P_L}$, where A represents the irradiated area, T_s represents the steady-state

temperature, T_0 represents the initial temperature, P_L represents the light power. The specific calculations are described in Note S3 (Supporting Information). We have measured the steady-state temperature of the M21C9 composite film under different light power densities, as shown in Fig. S17 (Supporting Information). Based on the results, the photothermal conversion efficiencies of the M21C9 composite film under the light power densities of 50, 100, 150, 200, 250, and 300 mW cm^{-2} were calculated to be 84.5%, 84.2%, 81.7%, 80.1%, 80.5%, and 81.1%, respectively. This demonstrates that it can efficiently convert light energy into thermal energy, which is promising to be utilized as an ideal photothermal layer. As shown in Fig. S18a (Supporting Information), a PTE performance measurement structure based on a U-shape frame was designed for preliminary investigation of the static PTE performance of the MCHF/PET/PEDOT:PSS bilayer film. A copper foil was attached directly to the upper end of the bilayer film as a photomask for constructing the temperature difference necessary for thermoelectric signal generation. As can be seen, the surface temperature of the MCHF/PET/PEDOT:PSS bilayer film increased with the increase in NIR light power density (Fig. S18b, Supporting Information). When the light power density reached 300 mW cm^{-2}, the maximum temperature difference and output voltage of the bilayer film reached 30.4 K and 0.737 mV, respectively. Besides, the temperature difference and output voltage trends of the MCHF/PET/PEDOT:PSS bilayer film are in good consistency (Fig. S18c-e, Supporting Information). After linear fitting calculation, the Seebeck coefficient of the MCHF/PET/PEDOT:PSS bilayer film during the static PTE performance measurement was 23.1 μV K^{-1} (Fig. S18f, Supporting Information).

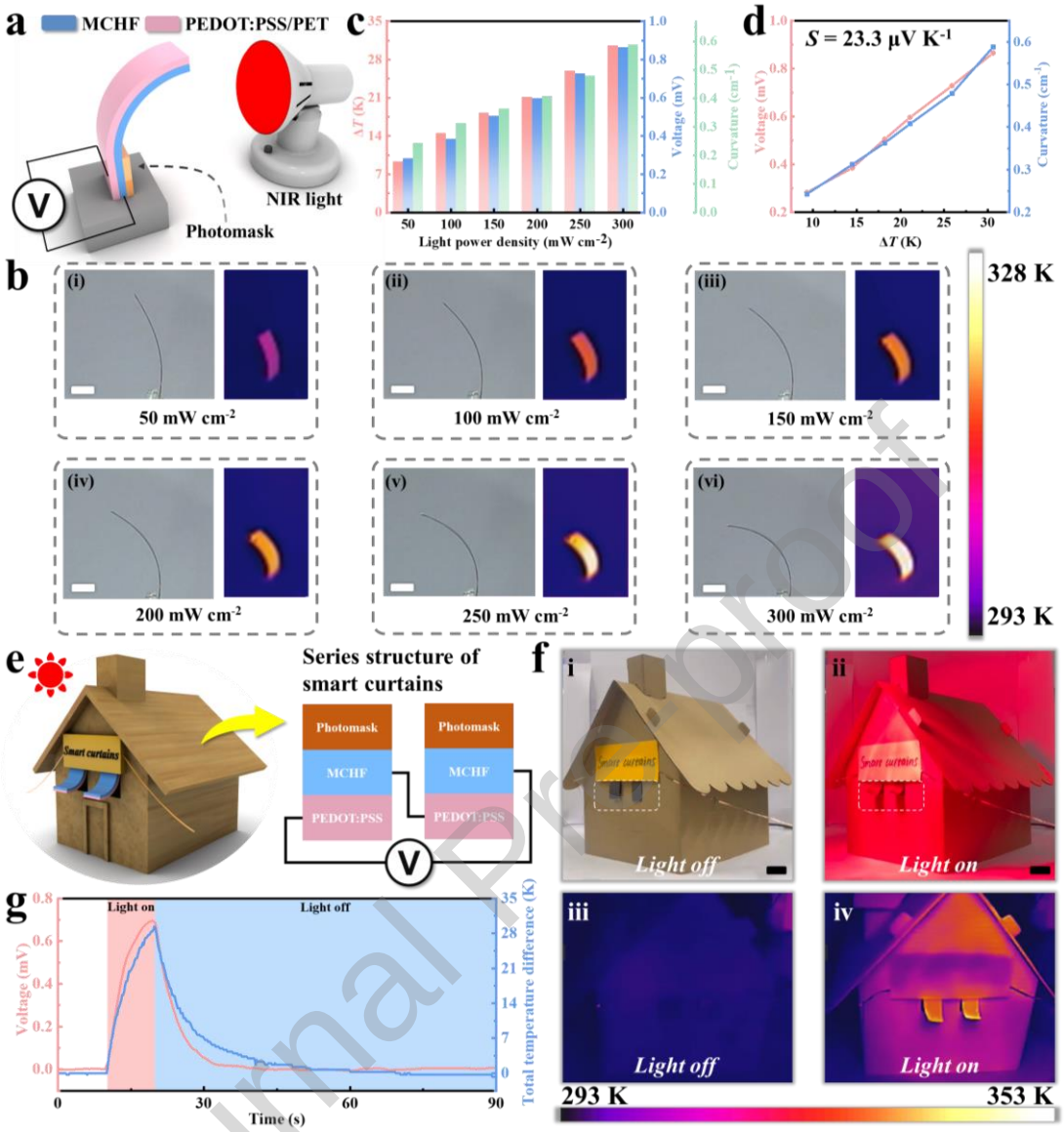

Fig. 4 Demonstration of the light-driven actuation and dynamic PTE performance of the MCHF/PET/PEDOT:PSS-based PTE actuator with relative-temperature perception. (a) Schematic illustration of the light-driven actuation and dynamic PTE performance measurement structure. (b) Optical photos and corresponding infrared thermal images of the MCHF/PET/PEDOT:PSS-based PTE actuator under different light power densities. (c) Output voltage, temperature difference, and curvature of the MCHF/PET/PEDOT:PSS-based PTE actuator under different light power densities. (d) Output voltage and curvature of the MCHF/PET/PEDOT:PSS-based PTE actuator versus temperature

difference. (e) Schematic illustration of the operation and "P-N-P" series structure of the smart curtains based on the MCHF/PET/PEDOT:PSS-based PTE actuators. (f) Optical photos (i-ii) and corresponding infrared thermal images (iii-iv) of the smart curtains before and after NIR light illumination. (g) The self-powered voltage signal and the corresponding comprehensive temperature difference generated spontaneously by the smart curtains during operation.

Subsequently, we attempted to further explore the synergistic effect between the light-driven actuation and self-powered perception of the MCHF/PET/PEDOT:PSS-based PTE actuator by altering the measurement structure based on the aforementioned static PTE performance measurement, as shown in Fig. 4a and Fig. S19 (Supporting Information). The calculation method for the bending curvature of the actuator is shown in Note S4 (Supporting Information) and Fig. S20 (Supporting Information). Fig. 4b illustrates the simultaneous recording of surface temperature changes and light-driven deformation states using an infrared thermal imager and a camera, respectively. It can be seen that the higher the surface temperature of the light-driven actuator, the more significant is its light-driven deformation toward the MCHF layer. Two mechanisms primarily contribute to the light-driven bending deformation of the MCHF/PET/PEDOT:PSS-based PTE actuators. One is the volume change mismatch due to the asymmetric thermal expansion effect between the MCHF layer and the PEDOT:PSS/PET layer. The other is the volume contraction due to the thermal-dehydration effect of the hydrophilic porous structure of the MCHF layer. From Fig. 4c and Fig. S21 (Supporting Information), it can be seen that the temperature difference, output voltage, and bending

curvature of the MCHF/PET/PEDOT:PSS-based PTE actuator maintained good consistency, similar to the aforementioned static PTE measurement. At ΔT = 30.6 K, the maximum voltage and bending curvature of the MCHF/PET/PEDOT:PSS-based PTE actuator can reach 0.865 mV and 0.59 cm^{-1}, respectively. This demonstrates that the light-driven actuation and the self-powered relative-temperature perception functions of the actuator can synergize without interfering with each other. And the Seebeck coefficient of 23.3 $\mu V\ K^{-1}$ is basically the same compared to the data obtained from the direct thermal contact measurement (24.5 $\mu V\ K^{-1}$) and static PTE measurement (23.1 $\mu V\ K^{-1}$) previously, as shown in Fig. 4d. As long as one of the parameters (ΔT, output voltage or curvature) is known, we can roughly derive the other two parameters according to the linear relationship (Fig. S22, Supporting Information) and the Seebeck coefficient. This characterization is very meaningful for self-powered perception applications of the MCHF/PET/PEDOT:PSS-based PTE actuator. Considering that the temperature difference change is dynamic rather than static in practical applications, we further performed a continuous dynamic heating of the MCHF/PET/PEDOT:PSS bilayer film by using a heating platform for proximity and separation to better present the relationship between the actual curve and the fitted curve (Fig. S23, Supporting Information). The results demonstrate that the actual curves of the temperature difference and output voltage of the MCHF/PET/PEDOT:PSS bilayer film follow the linear fitting curve well. Moreover, we performed a 300-cycle irradiation test on the MCHF/PET/PEDOT:PSS-based light-driven actuator to explore whether it can maintain excellent per-

formance over long-term operation. As can be seen in Fig. S24 (Supporting Information), the maximum temperature-difference change rate, maximum voltage change rate, and maximum curvature change rate of the MCHF/PET/PEDOT:PSS-based light-driven actuator exhibited no significant degradation during the 300-cycle irradiation test. This demonstrates the excellent stability and durability of the MCHF/PET/PEDOT:PSS light-driven actuator.

Based on the mutually unaffected light-driven deformation and self-powered output capabilities of the MCHF/PET/PEDOT:PSS-based PTE actuator, we further designed a type of smart curtains that can autonomously perceive temperature changes. Two MCHF/PET/PEDOT:PSS-based PTE actuators were assembled in a "P-N-P" series structure, and the temperature differences were created by using the copper tapes as the top photomasks, as shown in Fig. 4e and Fig. S25 (Supporting Information). Since the MCHF layers possess excellent photothermal conversion performance, they were placed outside to absorb external light energy. Under weak light intensity conditions, the smart curtains presented a flat initial state with no obvious temperature change on the surface (Fig. 4f(i) and (iii)). Once the NIR light (~ 200 mW cm^{-2}) began to irradiate, the smart curtains rapidly bent towards the outside, thus allowing light to enter the room (Fig. 4f(ii) and (iv)). Furthermore, we simultaneously recorded the output voltage signal and the total temperature difference of the smart curtains during operation (Fig. 4g). As can be seen, the smart curtains can synchronize the output of self-powered voltage signals according to the temperature difference and deformation state when they perceive a drastic change in temperature. In the future, such energy-saving

smart curtains with self-perception functions can expand their practical application prospects in the field of smart homes by increasing the series number, actuation area, etc.

2.4 Triboelectric Output Performance of the MCHF-TENG

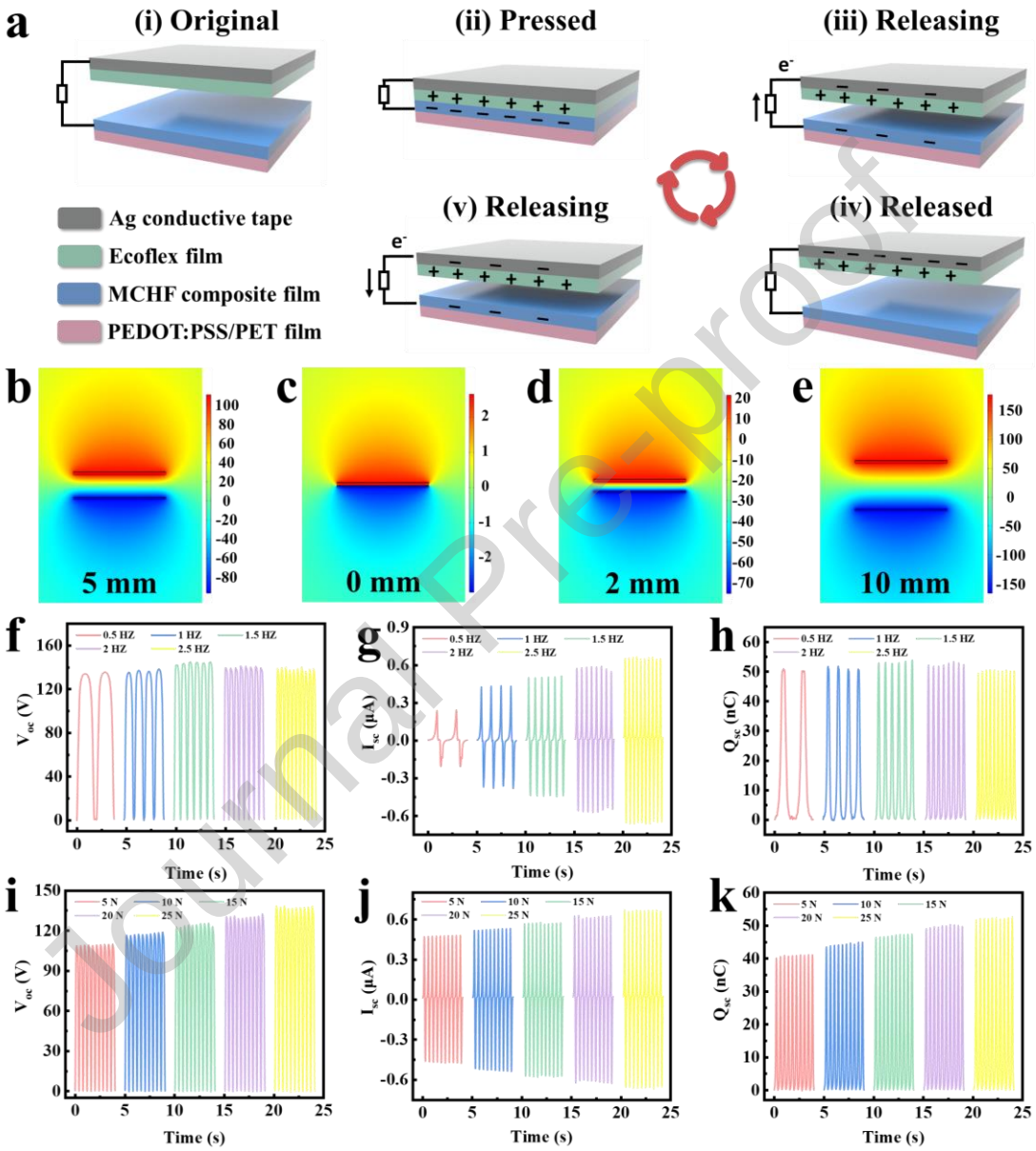

Fig. 5 Demonstration of the triboelectric output performance of the MCHF-TENG. (a) Schematic illustration of the working mechanism of the MCHF-TENG. FEM simulation of potential distributions between the two electrodes (b) 5 mm apart before contact,

(c) in contact, (d) 2 mm apart after contact, and (e) 10 mm apart, the maximum separation distance. Comparison of the triboelectric output performance of the MCHF-TENG with various contact-separation frequencies as a function of output open-circuit voltage (f), short-circuit current (g), and output short-circuit charge (h). Comparison of the triboelectric output performance of the MCHF-based TENG with various applied forces as a function of output open-circuit voltage (i), short-circuit current (j), and output short-circuit charge (k).

Different from the conventional PTE mechanism, the triboelectric effect is an emerging self-powered perception mechanism that can convert dynamic mechanical energy into electrical energy through the coupling of contact electrification and electrostatic induction [54]. And the CHF-modified MCHF composite film not only retains most of the conductive performance of $Ti_3C_2T_x$ MXene but also obtains excellent robustness. Hence, a contact-separation TENG was assembled with the MCHF/PET/PEDOT:PSS bilayer film as a triboelectric negative electrode to systematically evaluate the comprehensive triboelectric performance of the MCHF layer (Fig. 5a(i)). We refer to this as MCHF-TENG. Ecoflex, which has a large difference in electronegativity from the $Ti_3C_2T_x$ MXene-based electrode, was selected as the triboelectric positive electrode [29, 55]. Due to the electric field, a charge drift occurs inside the Ecoflex dielectric layer, resulting in an opposing induced field (Fig. 5a(ii)). When releasing the external force, the potential difference induces a directional electron movement between the MCHF/PET/PEDOT:PSS and the Ecoflex/Ag electrodes (Fig. 5a(iii)). The potential equilibrium state is achieved after the complete separation of the two electrode layers

(Fig. 5a(iv)). As the two electrodes reoccur in mutual contact under mechanical external force, the reconstructed potential difference induces electron flow back to the MCHF electrode layer (Fig. 5a(v)). The periodic contact-detachment driven by the linear motor causes a continuous electron movement between the MCHF and the Ecoflex electrodes, thus generating a low-frequency alternating current (AC). To verify the aforementioned analysis of the MCHF-TENG's working mechanism, finite element method (FEM) simulations of the potential changes were performed using the COMSOL software (Fig. 5b-e). Only two electrode plates, representing the MCHF electrode and the Ecoflex electrode, were used in the simulation for clarity. When the distance between the two electrode plates changes, the potential distribution on each electrode plate surface also changes. The resulting potential difference is proportional to the separation distance. For example, as the electrode plate distance decreases from 5 mm to 0 mm, the positive electrode potential decreases from 100 V to 0 V; as the electrode plate distance increases from 2 mm to 10 mm, the positive electrode potential spikes from 60 V to 150 V (the maximum simulated potential difference of the MCHF-TENG).

Subsequently, to evaluate the practical triboelectric output performance of the MCHF-TENG, the open-circuit voltage, short-circuit current, and charge of the MCHF-TENG were measured under different contact-detachment conditions, respectively. The triboelectric output performance of the MCHF-TENG was first measured at a contact-separation frequency of 0.5-2.5 Hz (constant contact force of 25 N), as shown in Fig. 5f-h. The MCHF-TENG achieved its maximum open-circuit voltage and short-circuit charge at 1.5 Hz frequency, with values of 144.7 V and 53.86 nC, respectively. While

the short-circuit current increases with the contact-separation frequency and reaches a maximum value of 0.66 μA at 2.5 Hz. We additionally measured the various output signals of the MCHF-TENG under different contact forces (constant contact-separation frequency of 2.5 Hz), as shown in Fig. 5i-k. The open-circuit voltage, short-circuit current, and short-circuit charge of MCHF-TENG all increase with the increase in contact force, and their maximum values can respectively reach 138.3 V, 0.67 μA, and 52.58 nC under 25 N. This is because the deeper degree of contact leads to a change in the energy bands, thus allowing more mechanical energy to be efficiently converted into electrical energy. Fig. S26 (Supporting Information) provides a more visual demonstration of the trend of the output signals of the MCHF-TENG. Moreover, we also measured the open-circuit voltage and short-circuit current of the MCHF-TENG under small-force conditions (0 kPa-5 kPa). The statistical measurement results are shown in Fig. S27 (Supporting Information). When the pressure was in the range of 0.1 kPa-1 kPa, the open-circuit voltage and short-circuit current of the MCHF-TENG increased linearly within 55.13 V kPa^{-1} and 0.27 μA kPa^{-1}, respectively. The sensitivity S is defined as $S = (\Delta V/V_s)/\Delta P$, where ΔV represents the relative change of open-circuit voltage, V_s represents the steady-state open-circuit voltage, and ΔP represents the external pressure [56, 57]. The MCHF-TENG can output voltage corresponding to the external pressure at a high sensitivity of about 0.51 kPa^{-1} under the small-force conditions. As shown in Table S1 (Supporting Information), we compared the comprehensive output performance between the MCHF-TENG and other contact-separation TENGs based on MXene-based composite films. The results demonstrate that the comprehensive output

performance of the MCHF-TENG belongs to the upper-middle level among the similar types of TENGs.

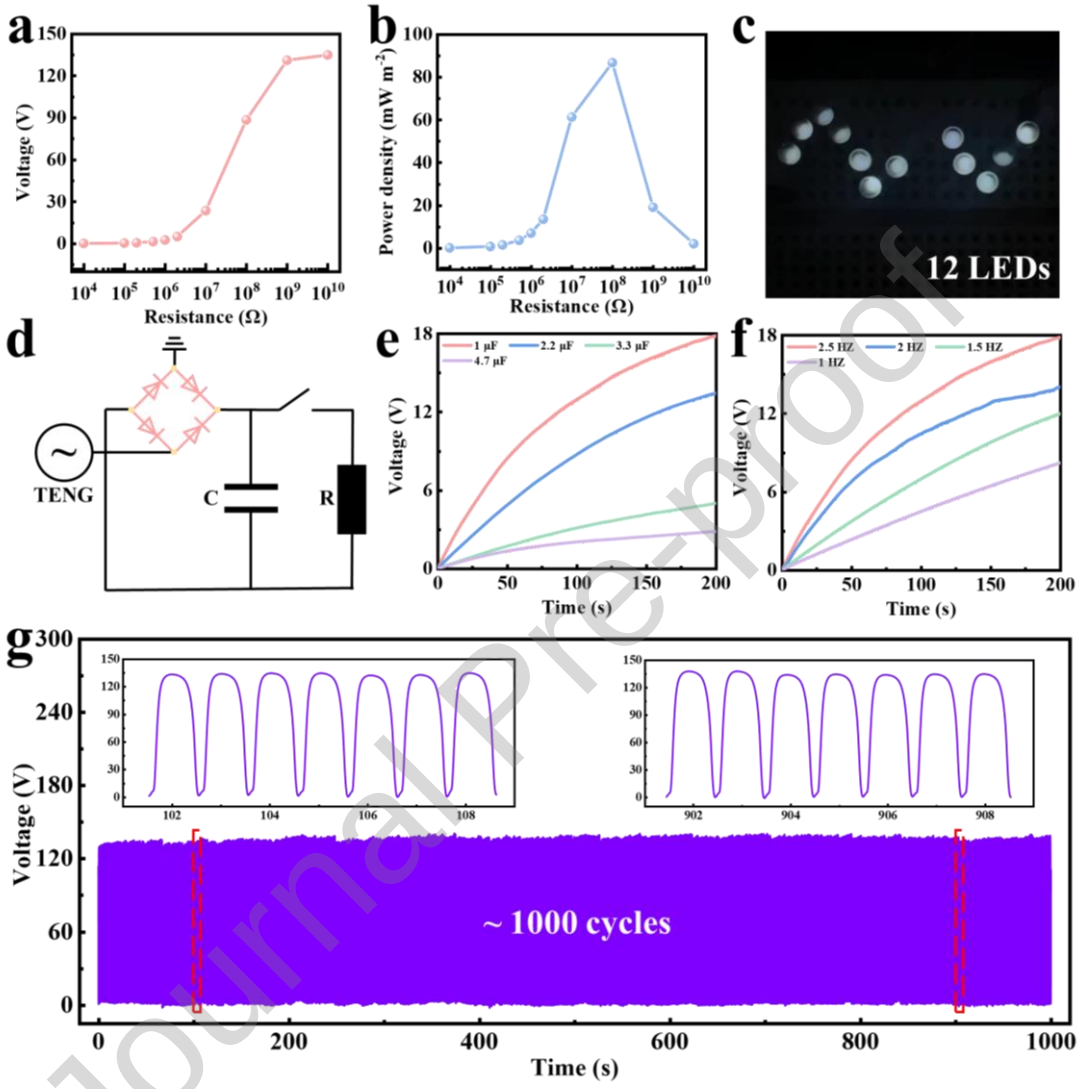

Fig. 6 Demonstration of the mechanical energy harvesting performance of the MCHF-TENG. (a) The output voltage of the MCHF-TENG as a function of the external load resistance. (b) The power density of the MCHF-TENG as a function of the external load resistance. (c) Optical photo of the LEDs driven by the MCHF-TENG. (d) Equivalent circuit of the self-charging system based on the MCHF-TENG. (e) Voltage charging curves of different capacitors charged by the MCHF-TENG. (f) Voltage charging curves

of the 1 μF capacitor charged by MCHF-TENG at different frequencies. (g) Cyclic stability of the MCHF-TENG.

To further evaluate the mechanical energy harvesting performance of the MCHF-TENG, we used it as a low-frequency AC power source and connected it to the load resistor of 10 KΩ-10 GΩ through the external circuit, as shown in Fig. 6a-b. As can be seen, the output voltage increases with the increase in the external load resistance. When the external load resistance is approaching the internal impedance (100 MΩ) of the MCHF-TENG, the instantaneous output power density can reach 86.69 mW m^{-2}. The MCHF-TENG can efficiently convert the mechanical energy collected from the linear motor system into low-frequency AC power to easily power multiple commercial LEDs (Fig. 6c). However, the high-entropy energy collected by MCHF-TENG is easily wasted and cannot directly drive most minor electronics. Thus, we designed a rectifier circuit, as shown in Fig. 6d. The output AC from MCHF-TENG is converted to DC by a bridge rectifier consisting of four rectifier diodes and then stored in a capacitor, for driving low-power electronics. The charging curves of the MCHF-TENG for charging capacitors of different capacities (1.0 μF, 2.2 μF, 3.3 μF, and 4.7 μF) at a contact-separation frequency of 2.5 Hz are illustrated in Fig. 6e. Wherein the MCHF can rapidly charge a 1 μF capacitor from 0 V to 18 V in 200 s. Fig. 6f displays the charging curves at various frequencies. These charging curves demonstrate that the MCHF-TENG can output efficient and stable power in a few hundred seconds. Additionally, the long-term mechanical energy harvesting performance of the MCHF-TENG (25N, 1 HZ) was measured, as shown in Fig. 6g. The MCHF-TENG can still maintain its output open-

circuit voltage at about 135 V after about 1000 cycles of contact-separation. In addition, the MCHF-TENG also exhibits fast response time and recovery time of 0.13 s and 0.24 s, respectively (Fig. S28, Supporting Information). This demonstrates the capability of the MCHF-TENG to sensitively convert mechanical excitation into voltage signals. Compared to other similar self-powered actuators, the MCHF/PET/PEDOT:PSS-based PTE/triboelectric actuators exhibit a relatively good comprehensive performance, as shown in Table S2 (Supporting Information).

2.5 Neural Network-Assisted Intelligent Gripper for Self-Powered Multi-Modal Perception

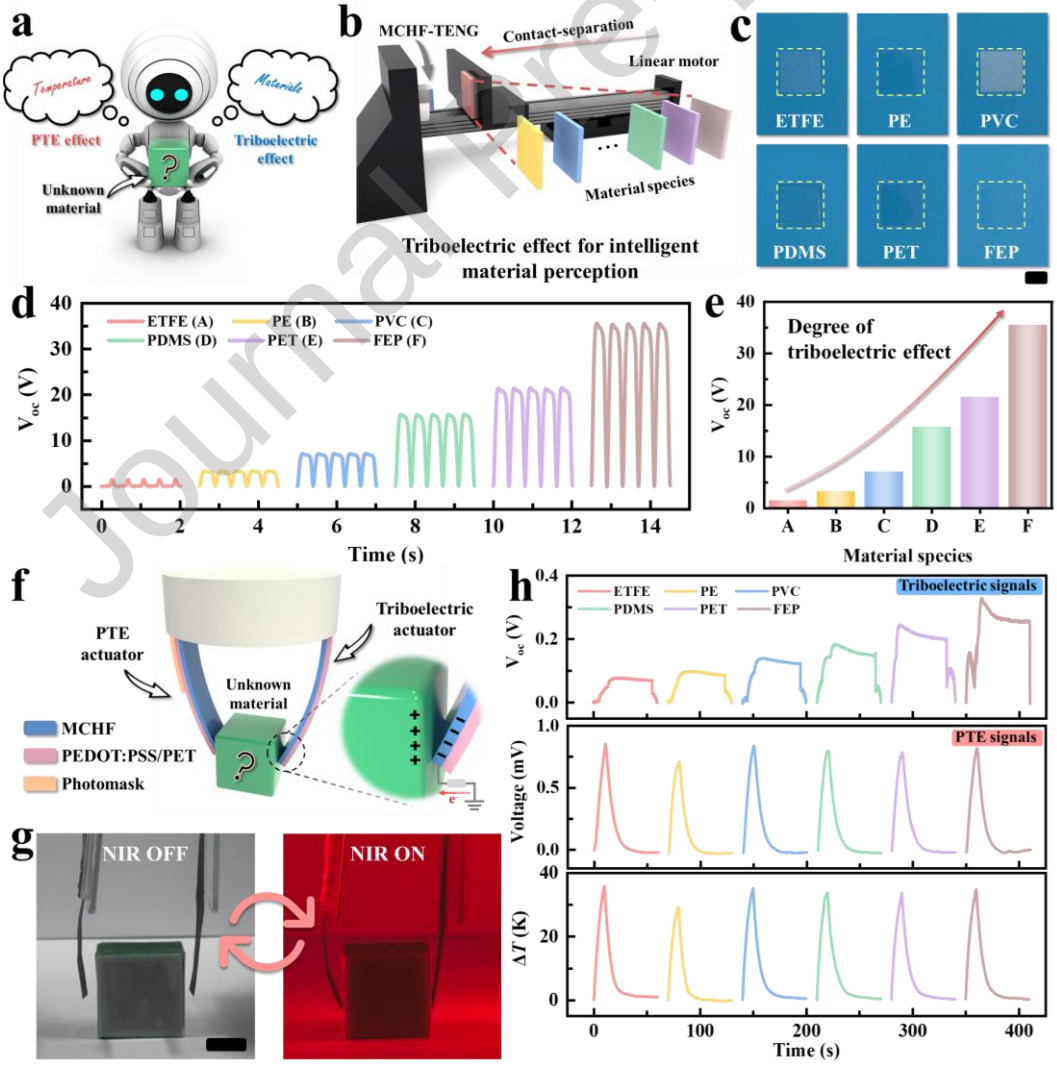

Fig. 7 Demonstration of the intelligent gripper for self-powered multi-modal perception. (a) Conceptual illustration of the designed intelligent gripper with multi-modal perception. (b) Schematic illustration of the intelligent measurement system for material perception performance. (c) Optical photos of six measured materials with the same contact area. Scale bar: 1 cm. (d) Output voltage signals generated by the MCHF-TENG in response to the six materials. (e) Summary of the maximum output voltage signals in response to the six materials. (f) Schematic illustration of the designed intelligent gripper with self-powered multi-modal perception. (g) Optical photos of the operation process of the intelligent gripper under NIR light. Scale bar: 1 cm. (h) The triboelectric voltage signals, PTE voltage signals, and temperature differences of the intelligent gripper when contacting six materials under NIR light irradiation.

Although conventional flexible actuators can accomplish mechanical deformation in response to external stimuli, the lack of multi-modal perception capability may limit the intelligent development of soft robots in robot-environment interaction [58]. Since the MCHF/PET/PEDOT:PSS bilayer film can be highly compatible with both the PTE and triboelectric effects, we proposed an "actuation-temperature perception-material perception" integrated strategy, trying to develop an actuation device that can spontaneously perceive multi-modal information without any external power source (Fig. 7a). First, to evaluate the material perception performance of the MCHF/PET/PEDOT:PSS bilayer film, a measurement system was constructed based on a charge transfer process in a single-electrode mode (Fig. 7b). Six different materials (ethylene tetra-fluoro-ethylene (ETFE), polyethylene (PE), polyvinyl chloride (PVC), polydimethylsiloxane

(PDMS), polyethylene terephthalate (PET), and fluorinated ethylene propylene (FEP)) with flat contact surfaces and the same area (2 cm × 2 cm) were selected as movable triboelectric electrodes to eliminate the effect of contact area on material perception performance (Fig. 7c). When different materials performed contact-separation motions under a constant driving condition (25N, 2.5Hz), the output voltage signals exhibited significant differences (Fig. 7d). Fig. 7e summarizes the maximum output voltages in response to the different materials, which more intuitively demonstrates the excellent material perception performance of the MCHF/PET/PEDOT:PSS bilayer film. The primary reason for this difference is that different materials possess different electron affinities, which means that electrons will be transferred from the material with the stronger affinity to the material with the weaker affinity [59, 60]. This charge transfer difference directly affects the degree of the triboelectric effect, which in turn affects the output voltage signals.

Based on the excellent material perception performance and the aforementioned triboelectric performance of the MCHF/PET/PEDOT:PSS bilayer film, we developed a triboelectric actuator. The triboelectric actuator can trigger triboelectric interactions with different materials by utilizing the contact force generated by the light-driven deformation. As shown in Fig. 7f and Fig. S29 (Supporting Information), we constructed an intelligent gripper by compactly assembling the PTE actuator and the triboelectric actuator in a symmetric manner. Different materials were attached to the surface of a 3D-printed cube (2 cm × 2 cm × 2 cm), and the cube was autonomously touched by the intelligent gripper under NIR light (Fig. 7g). The simultaneous collected triboelectric

signals, PTE signals, and temperature difference as the intelligent gripper contacts different materials are shown in Fig. 7h. As can be seen, the triboelectric perception signal trend (decrease from 0.329 V with FEP to 0.078 V with ETFE) of the triboelectric actuator in single-electrode mode in response to the contact materials remains consistent with the aforementioned measurement results. Moreover, the thermoelectric signals collected by the PTE actuator can also reflect the temperature difference according to the Seebeck coefficient (~23.3 μV K^{-1}). The above results demonstrate that the intelligent gripper can realize the synergetic effects of light-driven actuation and self-powered multi-modal perception without causing mutual interference between the two actuator components. To better demonstrate the sensitivity of light-driven actuation and multi-modal perception of the intelligent gripper in complex dynamic work, we used the NIR light to simulate different environmental temperatures to drive the intelligent gripper to move an object (Fig. S30, Supporting Information). Fig. S30a-c (Supporting Information) illustrate the optical photos of the moving object process of the intelligent gripper and the corresponding thermoelectric and triboelectric signals, respectively. Before irradiation (0 s-3 s), the intelligent gripper hardly deformed, and the corresponding thermoelectric and tribo-electric signal curves were relatively smooth. Once irradiation started, the thermoelectric and triboelectric signals output from the stimulated intelligent gripper began to increase rapidly. Benefiting from the excellent light-driven actuation performance, the intelligent gripper can steadily grasp the object twice its own weight in just 15 s (3 s - 18 s). After the intelligent gripper placed the object stably at the specified position (18 s-26 s), we stopped the NIR light irradiation. At this point,

the thermoelectric signal output from the intelligent gripper, which lost its light source, began to decrease rapidly. In contrast, the triboelectric signal remains at a relatively constant level as the intelligent gripper was still not separated from the object. Until the intelligent gripper completed the operation of releasing the object (26 s-35 s), the triboelectric signal decreased rapidly. This experiment well demonstrates the excellent sensitivity of the MCHF/PET/PEDOT:PSS-based intelligent gripper for light-driven actuation and multi-modal perception in complex dynamic work, further exhibiting its broadness in the field of soft robots.

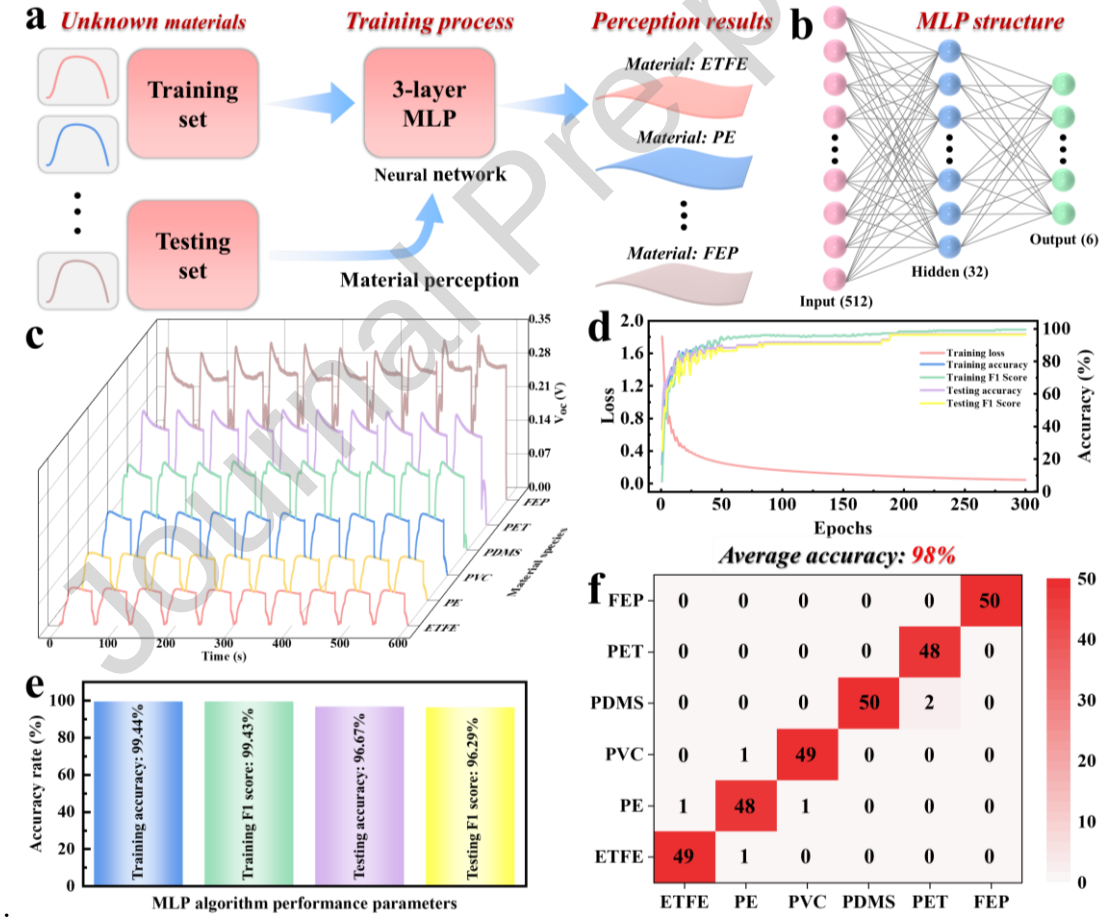

Fig. 8 Demonstration of the MLP neural network-assisted intelligent material perception system. (a) Operation flow of the three-layer MLP neural network-assisted intelligent material perception system. (b) Structure of the three-layer MLP neural network

algorithm model. (c) Partial triboelectric voltage signals collected by the intelligent gripper during cyclic contact-separation with the six different materials. (d) Curves of the training loss, training accuracy, training F1 score, accuracy, and test F1 score as a function of the epochs for the MLP neural network algorithm (Epoch = 300). (e) Values of the three-layer MLP neural network algorithm performance indicators after 300 epochs. (f) Confusion matrix of material classification results based on the three-layer MLP neural network algorithm.

The intelligent gripper typically operates in an open environment. Many dynamically changing environmental factors (e.g. temperature, humidity, and autonomous contact force) as well as the triboelectric properties of different materials will affect the signal characteristics (e.g. amplitude, duration time, and waveform) of the triboelectric actuator [61]. As a result, the triboelectric actuator cannot simply convert the output signals into material perception information by means of specific parameterization (e.g., the Seebeck coefficient of the PTE actuator). To address this challenge, we constructed a MLP neural network-assisted intelligent system that can realize material classification by extracting complex signal features, to help the intelligent gripper achieve high-precision multi-modal perception (Fig 7a-b). In practice, we employ a three-layer MLP with 512-32-6 hidden units, which requires minimal computational resources. Subsequently, triboelectric signals from six different materials were collected as a dataset using an intelligent gripper under constant periodic conditions (10 s irradiation, 50 s cooling), as shown in Fig. 8c. The selection of the MLP model as the algorithm for the

intelligent gripper was based on a careful analysis and practice of the data characteristics. Our task involved classifying materials based on voltage time-series data, but we found that the material species had a weak temporal dependence on the voltage series and a closer relationship with the static distribution of features at individual time points. This means that the overall distribution of voltage values at individual time points is more important in determining material species than continuity or patterns of change along the time dimension. Therefore, we treat the data as a high-dimensional static feature set and use the MLP model to capture the overall distribution of the captured voltage values, which matches the properties of our data. 50 sets of cyclic signals were collected for each material. 60%, 20%, and 20% of the samples were randomly split as training set, validation set, and test set. Specifically, the neural network was trained on the training set for 300 epochs, optimized using the validation set to obtain the best parameters, and finally evaluated on the test set. Fig. 8d displays the curves of training loss, training accuracy, training F1 score, testing accuracy, and testing F1 score for the MLP neural network algorithm after training. With only 50 epochs, the training loss of the MLP neural network algorithm can be reduced to less than 0.25, and the other four performance indicators trend to a horizontal state, indicating the convergence of the model. Finally, after 300 epochs, the MLP neural network algorithm can achieve excellent training accuracy, training F1 score, test accuracy, and test F1 score of 99.44%, 99.43%, 96.67%, and 96.29%, respectively (Fig. 8e). In real-world scenarios, collected samples of different materials may be imbalanced. Therefore, in addition to accuracy, we also use macro F1 scores to ensure a more comprehensive evaluation of system

performance. The excellent performance with respect to both accuracy and F1 scores demonstrates the proposed neural network-assisted intelligent material perception system's strong capability to distinguish different materials. As shown in Fig. 8f, the values in the confusion matrix are concentrated along the diagonal, indicating very few misclassified samples by the model, which corresponds to the excellent accuracy and F1 score. The average accuracy of the MLP neural network-assisted intelligent material recognition system can reach 98%. To further analyze the classification results, we mapped the low-dimensional embedding learned by the neural network of each sample into a two-dimensional space using the t-SNE algorithm for visualization [62]. As illustrated in Fig. S31 (Supporting Information), consistent with the confusion matrix, there may be a minimal number of misclassified samples between PE and ETFE, PE and PVC, and PET and PDMS due to the similarity in the electrical signal curves. Additionally, to increase the persuasiveness of the MLP-assisted material recognition system, polypropylene (PP), Kapton, and polytetrafluoroethylene (PTFE), which have much smaller differences in electronegativity (gradually increasing electronegativity from left to right), were selected for training with the previously tested ETFE and PE [63]. The test results of the contact-separation voltages in Fig. S32a-b (Supporting Information) visualize their close electronegativity. We collected the triboelectric signals of these five materials as a dataset using the intelligent gripper under the same cyclic conditions as before (Fig. S32c, Supporting Information). The training accuracy, training F1 score, testing accuracy, and testing F1 score can reach 100%, 100%, 98%, and 97.31% after 300 epochs, respectively (Fig. S32d-e, Supporting Information). With the

small electronegativity differences, the MLP neural network-assisted intelligent material recognition system can still achieve an average accuracy of 98.8%, as shown in Fig. S32f (Supporting Information). The above results demonstrate that the MLP neural network algorithm with strong fitting and generalization capabilities can help the intelligent gripper achieve high-accuracy multi-modal environmental perception while accomplishing light-driven actuation. Such an "actuation-temperature perception-material" integrated device is expected to provide new ideas for next-generation intelligent soft robots to enhance autonomous environmental perception and human-machine interaction capabilities.

3. Conclusion

Through vacuum-assisted self-assembly and in-situ attachment, we elaborately designed the MCHF/PET/PEDOT:PSS light-driven actuators with the P-N couple structure and demonstrated their potential application in self-powered multi-modal perception. First, by combining the light-driven actuation mechanism and the PTE effect, the MCHF/PET/PEDOT:PSS-based PTE actuator with a PTE Seebeck coefficient of 23.3 $\mu V\ K^{-1}$ and a bending curvature of 0.59 cm^{-1} was developed. Based on the mutually unaffected capabilities of light-driven deformation and voltage output, the PTE actuator can be utilized to design a smart curtain with autonomous environmental response and self-powered relative-temperature perception. Second, thanks to the electrical and robust properties of the MCHF composite film, the MCHF-TENG with the MCHF/PET/PEDOT:PSS bilayer film as the triboelectric electrode exhibits excellent

output performance (maximum output voltage of 144.7 V). Based on this, we have realized autonomous material perception by utilizing the light-driven actuation force of the MCHF/PET/PEDOT:PSS-based triboelectric actuator as a trigger for the triboelectric effect. Finally, as a highlight of this work, we developed an intelligent gripper that coordinates light-driven actuation and multi-mode (relative temperature/material) perception by compactly integrating the PTE actuator and the triboelectric actuator. Assisted by the stable Seebeck coefficient and MLP neural network, the intelligent gripper can convert the collected perceptual signals into effective environmental information with an accuracy of up to 98%. Looking ahead, the actuator structure of the P-N couple structure and the integrated "actuation-temperature perception-material perception" strategy proposed in this work are expected to provide new insights into the intelligent interaction between $Ti_3C_2T_x$ MXene-based soft robots and environments.

Acknowledgements

This work was supported by the National Natural Science Foundation of China [Grant number 52103138, 52201043], the Natural Science Foundation of Fujian Province [Grant number 2023J01159, 2022J01945], the STS Project of Fujian-CAS [2023T3043], and Starting Research Fund from Fujian University of Technology [GYZ220199].

References:

[1]D. Rus, M.T. Tolley, Design, fabrication and control of soft robots. Nature. 521 (7553) (2015) 467-475. 10.1038/nature14543

[2]M.W.M. Tan, H. Wang, D. Gao, P. Huang, P.S. Lee, Towards high performance

and durable soft tactile actuators. Chem. Soc. Rev. 53 (7) (2024) 3485-3535. 1 10.1039/d3cs01017a

[3] X. Yang, L. Lan, X. Pan, Di Q, X. Liu, L. Li, P. Naumov, H. Zhang, Bioinspired soft robots based on organic polymer-crystal hybrid materials with response to temperature and humidity. Nat. Commun. 14 (1) (2023) 2287. 10.1038/s41467-023-37964-1

[4] X.Q. Wang, K.H. Chan, Y. Cheng, T. Ding, T. Li, S. Achavananthadith, S. Ahmet, J.S. Ho, G.W. Ho, Somatosensory, light-driven, thin-film robots capable of integrated perception and motility. Adv. Mater. 32 (21) (2020) 2000351. 10.1002/adma.202000351

[5] J. Park, Y. Lee, S. Cho, A. Choe, J. Yeom, Y.G. Ro, J. Kim, D. Kang, S. Lee, H. Ko, Soft sensors and actuators for wearable human–machine interfaces. Chem. Rev. 124 (4) (2024) 1464-1534. 10.1021/acs.chemrev.3c00356

[6] D. Zhang, K. Yang, X. Liu, M. Luo, Z. Li, C. Liu, M. Li, W. Chen, X. Zhou, Boosting the photothermal conversion efficiency of MXene film by porous wood for light-driven soft actuators. Chem. Eng. J. 450 (2022) 138013. 10.1016/j.cej.2022.138013

[7] S. Ma, X. Li, S. Huang, J. Hu, H. Yu, A light-activated polymer composite enables on-demand photocontrolled motion: transportation at the liquid/air interface. Angew. Chem. Inter. Ed. 58 (9) (2019) 2655-2659. 10.1002/anie.201811808

[8] C. Li, X. Yang, Y. Wang, J. Liu, X. Zhang, Core–shell nanostructured assemblies enable ultrarobust, notch-resistant and self-healing materials. Adv. Funct. Mater. 34 (2024) 2410659. 10.1002/adfm.202410659

[9] M. Weng, P. Zhou, L. Chen, L. Zhang, W. Zhang, Z. Huang, C. Liu, S. Fan, Multiresponsive bidirectional bending actuators fabricated by a pencil-on-paper method. Adv. Funct. Mater. 26 (40) (2016) 7244-7253. 2 10.1002/adfm.201602772

[10] M. Weng, J. Zhou, P. Zhou, R. Shang, M. You, G. Shen, H. Chen, Multi-functional actuators made with biomass-based graphene-polymer films for intelligent gesture recognition and multi-mode self-powered sensing. Adv. Sci. 11 (22) (2024) 2309846. 10.1002/advs.202309846

[11] R.S. Sutar, S.S. Latthe, X. Wu, K. Nakata, R. Xing, S. Liu, A. Fujishima, Design and mechanism of photothermal soft actuators and their applications. J. Mater. Chem. A. 12 (29) (2024) 17896-17922. 1 10.1039/D4TA00544A

[12] P. Zhou, J. Lin, W. Zhang, Z. Luo, L. Chen, Pressure-perceptive actuators for tactile soft robots and visual logic devices. Adv. Sci. 9 (5) (2022) 2104270. 10.1002/advs.202104270

[13] L. Chen, M. Weng, P. Zhou, F. Huang, C. Liu, S. Fan, W. Zhang, Graphene-based actuator with integrated-sensing function. Adv. Funct. Mater. 29 (5) (2019) 1806057. 10.1002/adfm.201806057

[14] M. Guo, X. Yang, J. Yan, Z. An, L. Wang, Y. Wu, C. Zhao, D. Xiang, H. Li, Z. Li, H. Zhou, Anti-freezing, conductive and shape memory ionic glycerol-hydrogels with synchronous sensing and actuating properties for soft robotics. J. Mater. Chem. A. 1 (3) (2022) 1615-1695. 1 10.1039/d2ta02576k

[15] H. Feng, P. Zhou, Q. Peng, M. Weng, Soft multi-layer actuators integrated with the functions of electrical energy harvest and storage. Chem. Eur. J. 30 (2024) 2303378. 10.1002/chem.202303378

[16] M. Naguib, M. Kurtoglu, V. Presser, J. Lu, J. Niu, M. Heon, L. Hultman, Y. Gogotsi, M.W. Barsoum, Two-dimensional nanocrystals produced by exfoliation of Ti_3AlC_2. Adv. Mater. 23 (37) (2011) 4248-4253. 10.1002/adma.201102306

[17] D. Xu, Z. Li, L. Li, J. Wang, Insights into the photothermal conversion of 2d MXene nanomaterials: synthesis, mechanism, and applications. Adv. Funct. Mater. 30 (47) (2020) 2000712. 10.1002/adfm.202000712

[18] V.H. Nguyen, R. Tabassian, S. Oh, S. Nam, M. Mahato, P. Thangasamy, A. Rajabi Abhari, W.J. Hwang, A.K. Taseer, I.K. Oh, Stimuli-responsive MXene-based actuators. Adv. Funct. Mater. 30 (47) (2020) 1909504. 1 10.1002/adfm.201909504

[19] S. Zeng, Y. Ye, P. Zhou, S. Yi, Q. Guo, H. Chen, G. Shen, M. Weng, Programmable and reconfigurable humidity-driven actuators made with mxene (Ti3C2Tx)-cellulose nanofiber composites for biomimetic applications. Nano Res. 17 (7) (2024) 6619-6629. 10.1007/s12274-024-6542-4

[20] Y. Hu, L. Yang, Q. Yan, Q. Ji, L. Chang, C. Zhang, J. Yan, R. Wang, L. Zhang, G. Wu, J. Sun, B. Zi, W. Chen, Y. Wu, Self-locomotive soft actuator based on asymmetric microstructural Ti3C2Tx MXene film driven by natural sunlight fluctuation. ACS Nano. 15 (3) (2021) 5294-5306. 10.1021/acsnano.0c10797

[21] Z. Jiao, Z. Hu, Y. Shi, K. Xu, F. Lin, P. Zhu, W. Tang, Y. Zhong, H. Yang, J. Zou, Reprogrammable, intelligent soft origami LEGO coupling actuation, computation, and sensing. Innovation. 5 (1) (2024) 100549. 10.1016/j.xinn.2023.100549

[22] X. Xiao, H. Ma, X. Zhang, Flexible photodriven actuator based on gradient-paraffin-wax-filled Ti3C2Tx MXene film for bionic robots. ACS Nano. 15 (8) (2021) 12826-12835. 1 10.1021/acsnano.1c03950

[23] Y. Zhong, H. Fang, Y. Ran, H. Zhu, Fast optical-writing recognition based on two-dimensional photothermoelectric effect assisted with deep learning. InfoMat. 5 (3) (2023) e12384. 10.1002/inf2.12384

[24] B. Kim, M. Han, E. Kim, Photothermally powered conductive films for absorber-free solar thermoelectric harvesting. J. Mater. Chem. A. 7 (5) (2019) 2066-2074. 1 10.1039/C8TA10399B

[25] P. Zhou, J. Lin, W. Zhang, Z. Luo, L. Chen, Photo-thermoelectric generator integrated in graphene-based actuator for self-powered sensing function. Nano Res. 15 (6) (2022) 5376-5383. 10.1007/s12274-021-3791-3

[26] W. Gu, P. Zhou, W. Zhang, Z. Luo, L. Chen, Pencil-drawn generator built-in actuator for integrated self-powered/visual dual-mode sensing functions and rewritable display. Adv. Sci. 10 (7) (2023) 2206467. 10.1002/advs.202206467

[27] K. Yang, J. Lin, C. Fu, J. Guo, J. Zhou, F. Jiao, Q. Guo, P. Zhou, M. Weng, *M*ultifunctional actuators integrated with the function of self-powered temperature sensing made with $ti_3c_2\ t_x$ –bamboo nanofiber composites. Nanoscale. 15 (46) (2023) 18842-18857. 10.1039/D3NR03885H

[28] K. Dong, X. Peng, Z.L. Wang, Fiber/fabric-based piezoelectric and triboelectric nanogenerators for flexible/stretchable and wearable electronics and artificial intelligence. Adv. Mater. 32 (5) (2020) e1902549. 10.1002/adma.201902549

[29] X. Cai, Y. Xiao, B. Zhang, Y. Yang, J. Wang, H. Chen, G. Shen, Surface control and electrical tuning of MXene electrode for flexible self-powered human-machine interaction. Adv. Funct. Mater. 33 (43) (2023) 2304456. 10.1002/adfm.202304456

[30] X. Huang, B. Zhou, G. Sun, X. Yang, Y. Wang, X. Zhang, Upcycling of plastic wastes and biomass to mechanically robust yet recyclable energy-harvesting materials. Nano Energy. 116 (2023) 108843. 10.1016/j.nanoen.2023.108843

[31] Y. Dong, S.S.K. Mallineni, K. Maleski, H. Behlow, V.N. Mochalin, A.M. Rao, Y. Gogotsi, R. Podila, Metallic MXenes: a new family of materials for flexible triboelectric nanogenerators. Nano Energy. 44 (2018) 103-110. 1 10.1016/j.nanoen.2017.11.044

[32] J. Chen, Y. Ding, D. Yan, J. Huang, S. Peng, Synthesis of MXene and its application for zinc-ion storage. SusMat. 2 (3) (2022) 293-318. 10.1002/sus2.57

[33] L. Xu, F. Xue, H. Zheng, Q. Ji, C. Qiu, Z. Chen, X. Zhao, P. Li, Y. Hu, Q. Peng, X. He, An insect larvae inspired MXene-based jumping actuator with controllable motion powered by light. Nano Energy. 103 (2022) 107848. 10.1016/j.nanoen.2022.107848

[34] P. Xue, H.K. Bisoyi, Y. Chen, H. Zeng, J. Yang, X. Yang, P. Lv, X. Zhang, A. Priimagi, L. Wang, X. Xu, Q. Li, Near-infrared light-driven shape-morphing of programmable anisotropic hydrogels enabled by MXene nanosheets. Angew. Chem. Inter. Ed. 60 (7) (2021) 3390-3396. 10.1002/anie.202014533

[35] X. Xiao, H. Ma, X. Zhang, Flexible photodriven actuator based on gradient–paraffin-wax-filled ti3c2 tx MXene film for bionic robots. ACS Nano. 15 (8) (2021) 12826-12835. 10.1021/acsnano.1c03950

[36] L. Li, Q. Cheng, MXene based nanocomposite films. Exploration. 2 (4) (2022). 10.1002/EXP.20220049

[37] R.A. Soomro, P. Zhang, B. Fan, Y. Wei, B. Xu, Progression in the oxidation stability of MXenes. Nano-Micro Lett. 15 (1) (2023) 108. 10.1007/s40820-023-01069-7

[38] W. Zhang, X. Ji, M. Ma, Emerging MXene/cellulose composites: design strategies and diverse applications. Chem. Eng. J. 458 (2023) 141402. https://doi.org/10.1016/j.cej.2023.141402

[39] J. Wang, Y. Liu, Z. Cheng, Z. Xie, L. Yin, W. Wang, Y. Song, H. Zhang, Y. Wang, Z. Fan, Highly conductive MXene film actuator based on moisture gradients. Angew. Chem. Inter. Ed. 59 (33) (2020) 14029-14033. 10.1002/anie.202003737

[40] J. Li, Z. Hao, B. Wang, X. Feng, Z. Mao, X. Sui, High-tensile chitin films regenerated from cryogenic aqueous phosphoric acid. Carbohydr. Polym. 312 (2023) 120826. 10.1016/j.carbpol.2023.120826

[41] S. Li, B. Gu, X. Li, S. Tang, L. Zheng, E. Ruiz Hitzky, Z. Sun, C. Xu, X. Wang, MXene-enhanced chitin composite sponges with antibacterial and hemostatic activity for wound healing. Adv. Healthc. Mater. 11 (12) (2022) 2102367. 10.1002/adhm.202102367

[42] V.E.Y.P. Irina P. Dobrovolskaya, E.M.I.K. Popryadukhin, P.M. A. Kasatkin, Effect of chitin nanofibrils on electrospinning of chitosan-based composite nanofibers. Carbohydr. Polym. 194 (2018) 260-266. 10.1016/j.carbpol.2018.03.074

[43] Y. Zhu, J. Liu, T. Guo, J.J. Wang, X. Tang, V. Nicolosi, Multifunctional $ti_3c_2t_x$ MXene composite hydrogels with strain sensitivity toward absorption-dominated electromagnetic-interference shielding. ACS Nano. 15 (1) (2021) 1465-1474. 10.1021/acsnano.0c08830

[44] D. Li, Q. Yuan, L. Huang, W. Zhang, W. Guo, M. Ma, Preparation of flexible n-doped carbon nanotube/MXene/PAN nanocomposite films with improved electrochemical properties. Ind. Eng. Chem. Res. 60 (42) (2021) 15352-15363. 10.1021/acs.iecr.1c03182

[45] Y.W.Y.Y. Chuchu Chen, T.Y.D.L. Pan, High strength gelatin-based nanocomposites reinforced by surface-deacetylated chitin nanofiber networks. Carbohydr. Polym. 195 (2018) 387-392. 10.1016/j.carbpol.2018.04.095

[46] M. Weng, M. Ding, P. Zhou, Y. Ye, Z. Luo, X. Ye, Q. Guo, L. Chen, Multi-functional and integrated actuators made with bio-inspired cobweb carbon nanotube-polymer composites. Chem. Eng. J. 452 (2023) 139146. 10.1016/j.cej.2022.139146

[47] T. Ma, Q. Zhou, L. Li, M. Pan, C. Guo, C. Mei, Nacre-inspired intumescent flame retardant bridging network for intelligent fire warning and prevention. Chem. Eng. J.

468 (2023) 143786. 10.1016/j.cej.2023.143786

[48] P. Dixit, S.S. Jana, T. Maiti, Enhanced thermoelectric performance of rare-earth-free n-type oxide perovskite composite with graphene analogous 2d MXene. Small. 19 (22) (2023) 2206710. 10.1002/smll.202206710

[49] X. Lu, Q. Zhang, J. Liao, H. Chen, Y. Fan, J. Xing, S. Gu, J. Huang, J. Ma, J. Wang, L. Wang, W. Jiang, High-efficiency thermoelectric power generation enabled by homogeneous incorporation of MXene in (Bi,Sb)2Te3 matrix. Adv. Energy Mater. 10 (2) (2020) 1902986. 10.1002/aenm.201902986

[50] Q. Li, X. Xu, J. Guo, J.P. Hill, H. Xu, L. Xiang, C. Li, Y. Yamauchi, Y. Mai, Two-dimensional MXene-polymer heterostructure with ordered in-plane mesochannels for high-performance capacitive deionization. Angew. Chem. Inter. Ed. 60 (51) (2021) 26528-26534. 10.1002/anie.202111823

[51] N. Liu, L. Yu, B. Liu, F. Yu, L. Li, Y. Xiao, J. Yang, J. Ma, Ti3c2 -MXene partially derived hierarchical 1d/2d TiO2/Ti3C2 heterostructure electrode for high-performance capacitive deionization. Adv. Sci. 10 (2) (2023) 2204041. 10.1002/advs.202204041

[52] M. Weng, J. Zhou, Y. Ye, H. Qiu, P. Zhou, Z. Luo, Q. Guo, Self-chargeable supercapacitor made with MXene-bacterial cellulose nanofiber composite for wearable devices. J. Colloid. Interface. Sci. 647 (2023) 277-286. 10.1016/j.jcis.2023.05.162

[53] Z. Wang, C. Zhang, Y. Li, J. Liang, J. Zhang, Z. Liu, C. Wan, P. Zong, Robustly enhanced seebeck coefficient in the MXene/organics/TiS2 misfit structure for flexible thermoelectrics. ACS Appl. Mater. Interfaces. 15 (30) (2023) 36301-36311. 10.1021/acsami.3c06680

[54] L. Liu, Y. Zhang, M. Wu, J. Zhang, L. Zhu, X. Zhou, J. Xiong, Asymmetric nanofiber photothermal interactive electronic skin with triboelectric autonomous thermal perceptivity. Nano Energy. 127 (2024) 109717. 10.1016/j.nanoen.2024.109717

[55] J. Zhou, H. Chen, P. Zhou, Q. Peng, Q. Guo, J. Wang, Y. Xu, M. You, M. Weng, Ti3C2Tx MXene nanosheet-functionalized leathers for versatile wearable electronics. ACS Appl. Nano Mater. 6 (19) (2023) 18150-18164. 10.1021/acsanm.3c03414

[56] S.G.S.L. Ying-Chih Lai, Breathable and stretchable multifunctional triboelectric

liquid-metal e-skin for recovering electromagnetic pollution, extracting biomechanical energy, and as whole-body epidermal self-powered sensors. Adv. Funct. Mater. 34 (10) (2024) 2312443. 10.1002/adfm.202312443

[57]T.L.M.L. Beibei Shao, Efficient permeable monolithic hybrid tribo-piezo-electro-magnetic nanogenerator based on topological-insulator-composite. Adv. Mater. 36 (41) (2024) 2408936. 10.1002/adma.202408936

[58]J. Zhou, Y. Zhang, J. Zhang, D. Zhang, X. Zhou, J. Xiong, Breathable metal–organic framework enhanced humidity-responsive nanofiber actuator with autonomous triboelectric perceptivity. ACS Nano. 17 (18) (2023) 17920-17930. 10.1021/acsnano.3c04022

[59]H. Niu, H. Li, S. Gao, Y. Li, X. Wei, Y. Chen, W. Yue, W. Zhou, G. Shen, Perception-to-cognition tactile sensing based on artificial-intelligence-motivated human full-skin bionic electronic skin. Adv. Mater. 34 (31) (2022). 10.1002/adma.202202622

[60]Q. Guo, J. Guo, H. Chen, P. Zhou, C. Li, K. Yang, N. Hua, J. Wang, M. Weng, Multi-functional graphene/leather for versatile wearable electronics. J. Mater. Chem. A. 11 (22) (2023) 11773-11785. 10.1039/D3TA01087B

[61]X. Wei, B. Wang, Z. Wu, Z.L. Wang, An open-environment tactile sensing system: toward simple and efficient material identification. Adv. Mater. 34 (29) (2022). 10.1002/adma.202203073

[62]G.H. Laurens Van Der Maaten, Visualizing data using t-SNE. J. Mach. Learn. Res. 9 (11) (2008) 2579-5605.

[63]D.K. Davies, Charge generation on dielectric surfaces. Journal of physics. D, Applied physics. 2 (11) (1969) 1533-1537. 10.1088/0022-3727/2/11/307

Declaration of Competing Interest

☒ The authors declare that they have no known competing financial interests or personal relationships that could have appeared to influence the work reported in this paper.

Graphical abstract

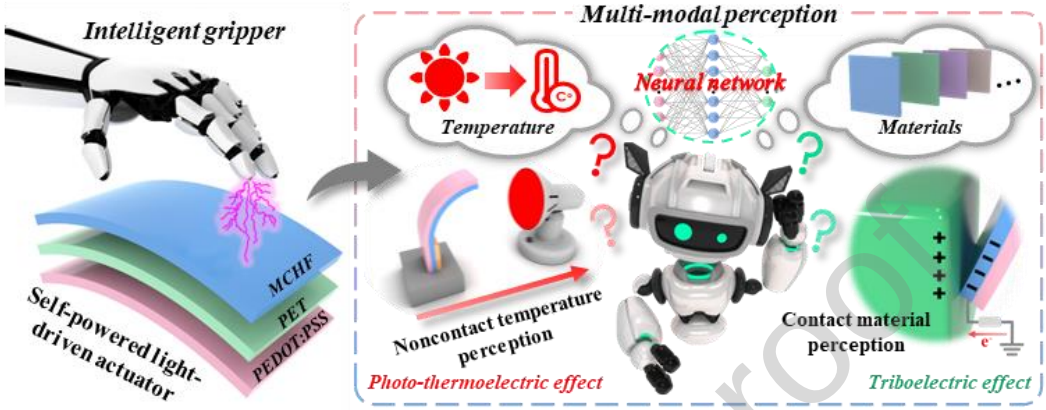

Highlights

- The MCHF/PET/PEDOT:PSS film possess bilayer P-N couple structure.
- The actuator can perceive relative temperature based on the Seebeck effect.
- The actuator can perceive materials based on the triboelectric effect.
- The intelligent gripper can perform self-powered multi-modal perception (98%) with the help of MLP neural network.
- The photo-thermal-electrical coupling mechanism is proposed for soft actuators with self-powered sensing functions.